

Supplementary Information

Highly Selective and Sensitive microRNA-210 Assay Based on Dual-Signaling Electrochemical and Photocurrent Polarity Switching Strategies

Qingqing Zhang, Suying Liu, Cuicui Du, Yamin Fu, Ke Xiao, Xiaohua Zhang, Jinhua Chen*

State Key Laboratory of Chemo/Biosensing and Chemometrics, College of Chemistry and Chemical Engineering, Hunan University, Changsha, 410082, P.R. China

List of Contents:

1. Materials and reagents
2. Apparatus
3. Preparation of DNA nanoprisms
4. XRD pattern of Fe-MOFs
5. TGA curve of Fe-MOFs
6. XRD pattern of Fe₃O₄ octahedra
7. HRTEM and EDS mapping images of Fe₃O₄@CdS octahedra
8. Nitrogen adsorption-desorption isotherms of Fe₃O₄ and Fe₃O₄@CdS octahedra

* Corresponding author. Tel.: +86-731-88821848

E-mail address: chenjinhua@hnu.edu.cn

- 9. Magnetic hysteresis loops of Fe_3O_4 and $\text{Fe}_3\text{O}_4@\text{CdS}$ octahedra**
- 10. Electrochemical and photoelectrochemical measurements**
- 11. The possible electron-transfer mechanisms of the $\text{MB}/\text{Fe}_3\text{O}_4@\text{CdS}/\text{ITO}$ and $\text{Dox}/\text{Fe}_3\text{O}_4@\text{CdS}/\text{ITO}$ electrodes**
- 12. Optimization of experimental conditions**
- 13. Photocurrent stability of the biosensing platform**
- 14. Comparison of different methods for miRNA-210 assay**
- 15. Recovery of miRNA-210 in the normal human serum samples**
- 16. Reference**

1. Materials and reagents

Doxorubicin hydrochloride (Dox) was bought from Macklin Reagent Co., Ltd. (China). 1,4-benzenedicarboxylic acid (BDC) was supplied by Aladdin Chemistry Co., Ltd. (China). Iron(III) chloride (FeCl_3), cadmium nitrate tetrahydrate ($\text{Cd}(\text{NO}_3)_2 \cdot 4\text{H}_2\text{O}$), sodium sulfide ($\text{Na}_2\text{S} \cdot 9\text{H}_2\text{O}$), tris-(hydroxymethyl) aminomethane (Tris), ethylenediaminetetraacetic acid (EDTA), potassium ferrocyanide ($[\text{K}_4\text{Fe}(\text{CN})_6]$), potassium ferricyanide ($[\text{K}_3\text{Fe}(\text{CN})_6]$), *N,N*-dimethylformamide (DMF), methanol (CH_3OH) were purchased from Sinopharm Chemical Reagent Co., Ltd. (China). Normal human serum was purchased from Anyan Inc. (China). All DNA and microRNA (miRNA) oligonucleotides were synthesized and HPLC-purified by Sangon Biotechnology Co., Ltd. (China) and their sequences were listed in Table S1. The ITO slices (coating thickness, 180 ± 25 nm; sheet resistance, $<10 \Omega \text{ sq}^{-1}$) were supplied by Zhuhai Kaivo Electronic Components Co., Ltd (China). Ultrapure water used in all experiments was obtained on a purification system from Wuhan Ulupure Pure Water Equipment Co., Ltd. (China).

Table S1. Sequences of oligonucleotides used in this work

Oligonucleotides	Sequence (5'-3')
miRNA-210	CUGUGCGUGUGACAGCGGCUGA
AP1	MB-TGACTACAACTTCAGCCGCTGT
AP2	MB-AGTTGTAGTCAACAGCGGCTGA
L	AGGCACCATCGTAGGTCTTGCCGGCACCATCGTA

GGTCTTGCCAGGCACCATCGTAGGTCTTGCC

CACACGCACAGTTCGATGGTGCCTGGCAAGACCT

Sa

TTCCGAACTGA

Sb

SH-CGATGGTGCCTGGCAAGACCTTTCAGTTCGGA

2. Apparatus

Fe-MOFs were synthesized on a microwave synthesizer (MAS-II Plus, Sineo, China). The morphologies and structures of the samples were characterized by scanning electron microscopy (SEM) (Hitachi S-4800, Japan) and transmission electron microscopy (TEM) (Tecnai G2 F20 S-TWIN, USA). X-ray diffractometer (XRD, D/MAX-RA, Japan) was used to analyze the crystalline phases of prepared materials. X-ray photoelectron spectroscopy (XPS, Thermo Scientific K-Alpha, USA) was used to analyze elemental composition and chemical status of the prepared materials. Thermal gravimetric analyzer (TGA, NETZSCH, Germany) was used to test the relationship between temperature and mass of the material ($10\text{ }^{\circ}\text{C}\cdot\text{min}^{-1}$, N_2). Automatic micropore and chemisorption analyzer (ASAP 2020, USA) was used to evaluate the Brunauer-Emmett-Teller (BET) surface area of the materials. The magnetic field dependent magnetization measurements were carried out on LakeShore7404 (USA). Photoelectrochemistry, electrochemical impedance spectroscopy (EIS) and square wave voltammetry (SWV) measurements were performed on an electrochemical workstation (CHI 660D, China) with a three-electrode system including a modified ITO electrode (diameter, 5.6 mm) as working electrode, a platinum wire as auxiliary electrode and a saturated calomel electrode (SCE) as reference electrode. Photoelectrochemical investigation was conducted with a 300 W Xe lamp fitted with a 420 nm UV filter (Perfect Light, Beijing) as irradiation source.

3. Preparation of DNA nanoprisms

The DNA nanoprisms were fabricated according to the reported work.¹ First, the strand L was mixed with the strand Sa (or Sb) with the molar ratio of L:Sa (or Sb) = 1:3 to get upper part (or bottom part). Then, the upper part and bottom part were mixed to generate the DNA nanoprisms. In final 100 μ L of DNA nanoprism solution, the final concentrations of L and Sa (or Sb) are 200 nM and 300 (or 300) nM, respectively.

Gel electrophoresis was used to confirm the formation of DNA nanoprisms. The polyacrylamide gel electrophoresis (PAGE) (8%) was carried out in 1 \times TAE buffer at a constant voltage of 80 V for 80 min at room temperature. After GelRed staining, the gel was photographed by gel image system.

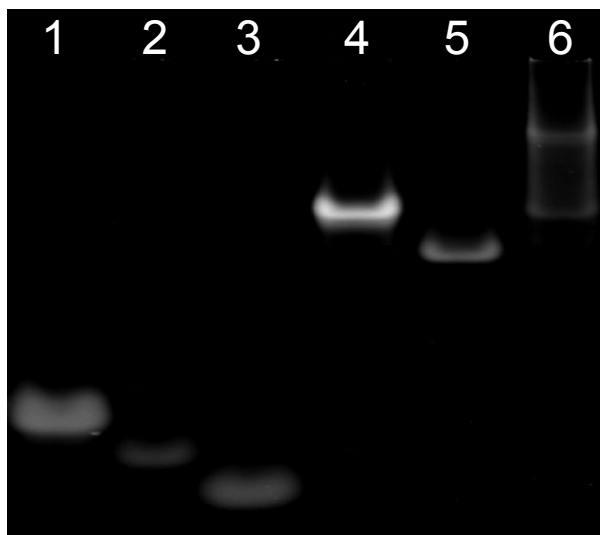


Figure S1. PAGE characterization for the assembly of DNA nanoprisms. lane 1: L; lane 2: Sa; lane 3: Sb; lane 4: L-Sa; lane 5: L-Sb; lane 6: DNA nanoprisms.

4. XRD pattern of Fe-MOFs

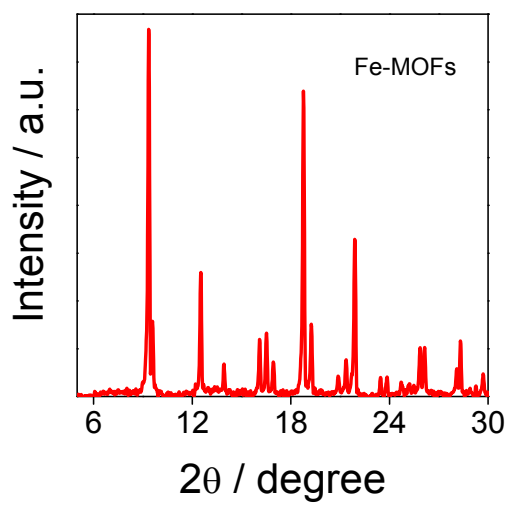


Figure S2. XRD pattern of Fe-MOFs.

5. TGA curve of Fe-MOFs

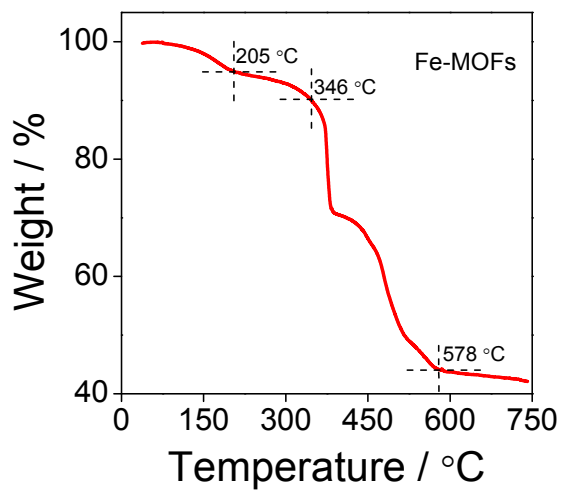


Figure S3. TGA curve of Fe-MOFs in N_2 .

6. XRD pattern of Fe_3O_4 octahedra

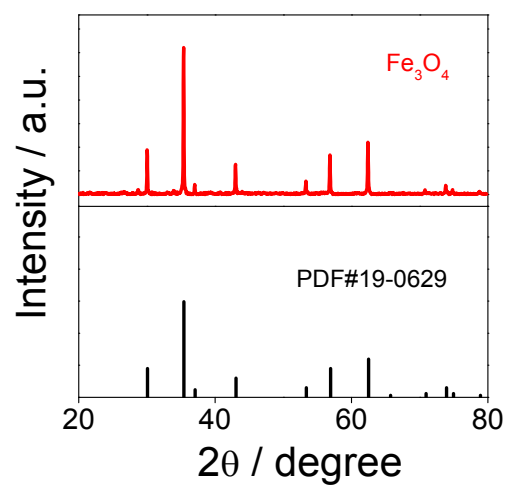


Figure S4. XRD pattern of Fe_3O_4 octahedra.

7. HRTEM and EDS mapping images of $\text{Fe}_3\text{O}_4@\text{CdS}$ octahedra

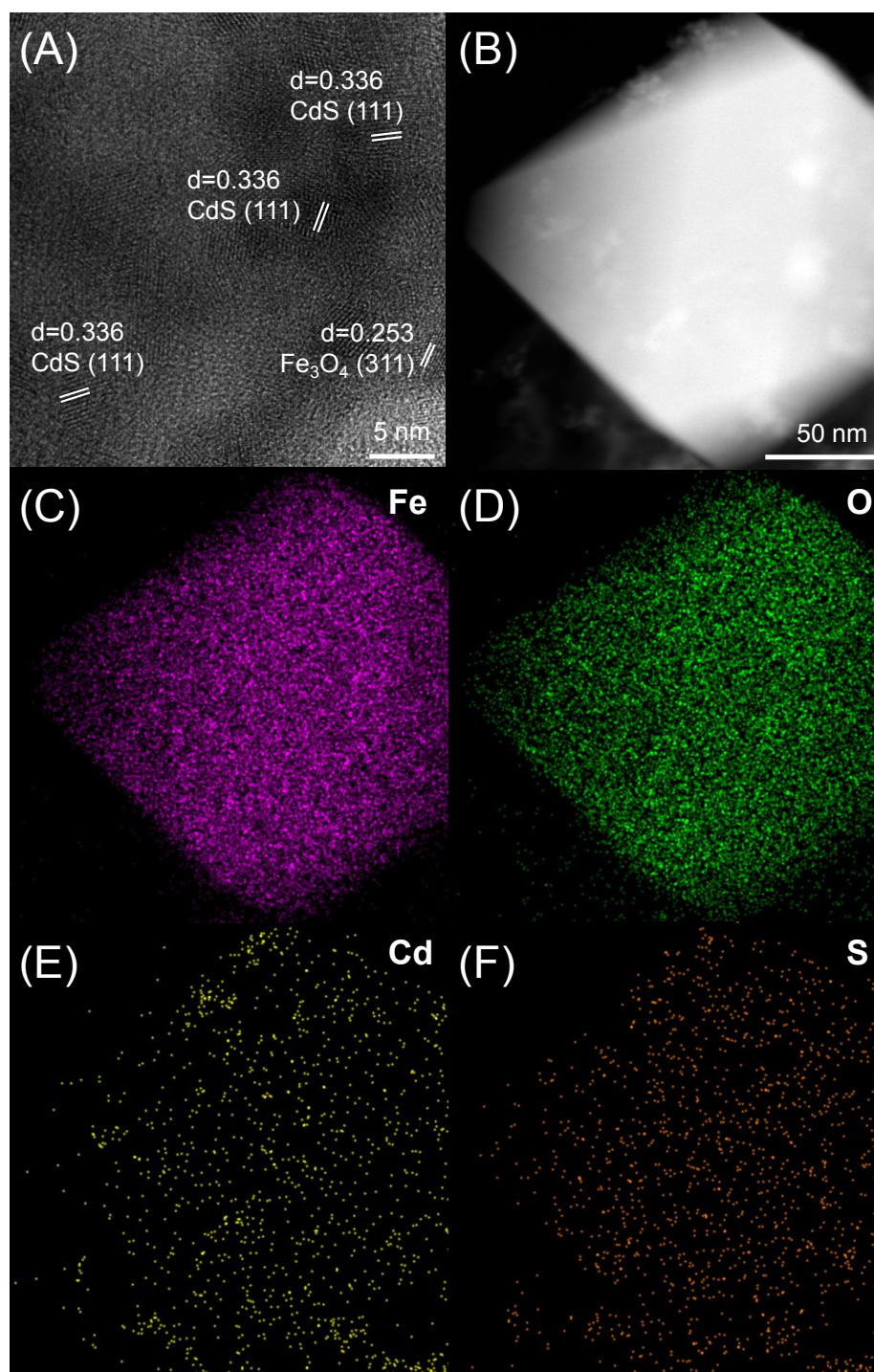


Figure S5. HRTEM and EDS mapping images of $\text{Fe}_3\text{O}_4@\text{CdS}$ octahedra.

8. Nitrogen adsorption-desorption isotherms of Fe_3O_4 and $\text{Fe}_3\text{O}_4@\text{CdS}$ octahedra

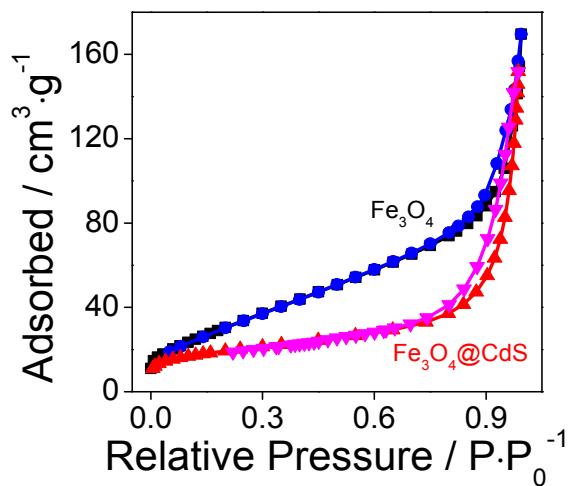


Figure S6. Nitrogen adsorption-desorption isotherms of Fe_3O_4 and $\text{Fe}_3\text{O}_4@\text{CdS}$ octahedra.

9. Magnetic hysteresis loops of Fe_3O_4 and $\text{Fe}_3\text{O}_4@\text{CdS}$ octahedra

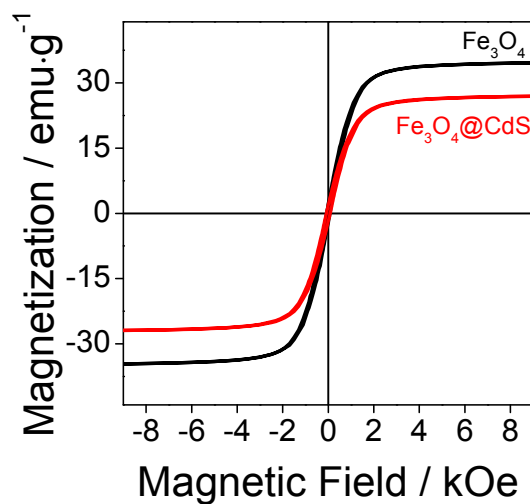


Figure S7. Magnetic hysteresis loops of Fe_3O_4 and $\text{Fe}_3\text{O}_4@\text{CdS}$ octahedra.

10. Electrochemical and photoelectrochemical measurements

The square wave voltammetry (SWV) responses were recorded in phosphate buffer (PBS) (100 mM, pH 7.4) from -0.80 to -0.15 V with a frequency of 15 Hz and an amplitude of 25 mV. And the electrochemical impedance spectroscopy (EIS) experiments were carried out in 0.1 M KCl aqueous solution containing 5 mM $[\text{Fe}(\text{CN})_6]^{3-/4-}$ (1:1) with a frequency range from 10^5 to 0.1 Hz and an amplitude of 5 mV. On the other hand, the photoelectrochemical assay was performed in PBS (100 mM, pH 7.4) at an applied potential of -0.3 V.

11. The possible electron-transfer mechanisms of the MB/Fe₃O₄@CdS/ITO and Dox/Fe₃O₄@CdS/ITO electrodes

The photoelectrochemical behaviors of the MB/Fe₃O₄@CdS/ITO and Dox/Fe₃O₄@CdS/ITO electrodes were investigated. From curve a in Figure S8A, it is noted that the Fe₃O₄@CdS/ITO electrode generates an anodic photocurrent. However, when the Fe₃O₄@CdS/ITO electrode is directly modified with MB (curve b) or Dox (curve c), a cathodic photocurrent is observed. The cathodic photocurrent of the MB/Fe₃O₄@CdS/ITO electrode is larger than that of the Dox/Fe₃O₄@CdS/ITO electrode, implying that MB has stronger photocurrent-polarity-switching ability than Dox. Furthermore, when the Fe₃O₄@CdS/ITO electrode is directly modified with the mixture of MB and Dox (curve d), a much large cathodic photocurrent is observed. It is noted that the cathodic photocurrent of the MB-Dox/Fe₃O₄@CdS/ITO is much larger than that of the MB/Fe₃O₄@CdS/ITO and Dox/Fe₃O₄@CdS/ITO electrodes, and also larger than the sum of their photocurrents, implying the synergistic effect between MB and Dox.

According to the conduction band (CB) and valence band (VB) edges of CdS,² and the highest occupied molecular orbitals (HOMO) and the lowest unoccupied molecular orbitals (LUMO) of Dox and MB,^{3,4} the possible photocurrent generation mechanisms of the MB/Fe₃O₄@CdS/ITO and Dox/Fe₃O₄@CdS/ITO electrodes are shown in Figure S8.

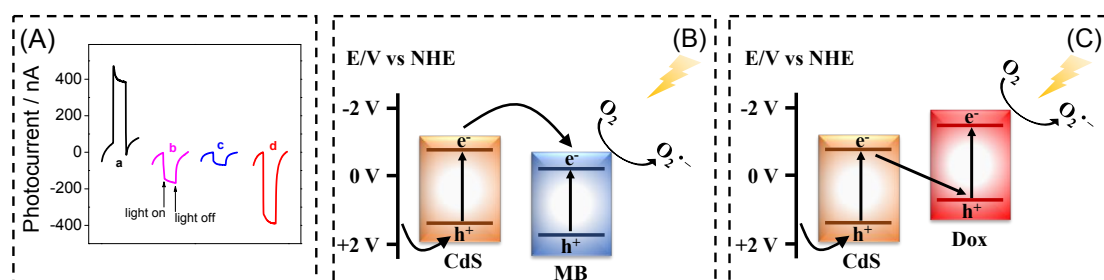


Figure S8 (A) Photocurrent responses of (a) Fe₃O₄@CdS/ITO, (b) MB/Fe₃O₄@CdS/ITO, (c) Dox/Fe₃O₄@CdS/ITO and (d) MB-Dox/Fe₃O₄@CdS/ITO electrodes. The possible electron-transfer mechanisms of (B) MB/Fe₃O₄@CdS/ITO and (C) Dox/Fe₃O₄@CdS/ITO electrodes.

12. Optimization of experimental conditions

The effects of the applied potentials on the photocurrents of the $\text{Fe}_3\text{O}_4@\text{CdS}/\text{ITO}$ and MB-Dox/ $\text{Fe}_3\text{O}_4@\text{CdS}/\text{ITO}$ electrodes have been investigated (Figure S9). It is noted that the anodic photocurrent of the $\text{Fe}_3\text{O}_4@\text{CdS}/\text{ITO}$ electrode increases when the applied potential shifts positively. On the other hand, for the MB-Dox/ $\text{Fe}_3\text{O}_4@\text{CdS}/\text{ITO}$ electrode, the cathodic photocurrent increases when the applied potential shifts negatively. It is well-known that the large applied potential (either positive or negative potential) may be not beneficial to the stability of the PEC sensor, and the anodic photocurrent of the $\text{Fe}_3\text{O}_4@\text{CdS}/\text{ITO}$ electrode and the cathodic photocurrent of the MB-Dox/ $\text{Fe}_3\text{O}_4@\text{CdS}/\text{ITO}$ electrode at -0.3 V are large enough for PEC assay, therefore, -0.3 V is selected as the optimal applied potential for all electrodes in this work.

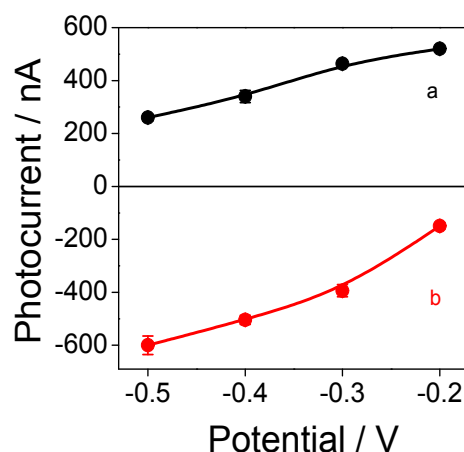


Figure S9. The effects of the applied potentials on the photocurrents of the $\text{Fe}_3\text{O}_4@\text{CdS}/\text{ITO}$ (a) and MB-Dox/ $\text{Fe}_3\text{O}_4@\text{CdS}/\text{ITO}$ (b) electrodes.

In order to obtain the optimal performance of the EC-PEC dual-mode biosensing

platform, the incubation time between miRNA-210 and DNA nanoprisms and the hybridization time of $[AP1+AP2]_n$ were optimized.

As shown in Figure S10A, it can be observed that both the $I_{Dox}+I_{MB}$ and photocurrent values of the dual-mode biosensing platform increase with the increase of the incubation time between miRNA-210 and DNA nanoprisms and then reach the plateaus at 1.5 h, indicating that the incubation process reaches equilibrium at 1.5 h. So, 1.5 h was selected as the optimal incubation time between miRNA-210 and DNA nanoprisms.

As shown in Figure S10B, it can be observed that both the $I_{Dox}+I_{MB}$ and photocurrent values of the dual-mode biosensing platform increase with the increase of the hybridization time of $[AP1+AP2]_n$ and then reach the plateaus at 2 h, implying that the hybridization process of AP1 and AP2 is completed at 2 h. Thus, 2 h is selected as the optimal hybridization time of $[AP1+AP2]_n$.

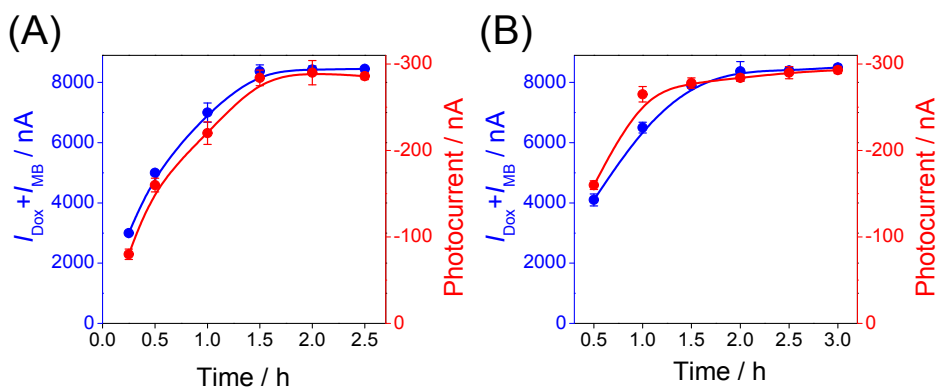


Figure S10. Effects of the incubation time between miRNA-210 and DNA nanoprisms (A) and hybridization time of $[AP1+AP2]_n$ (B) on the $I_{Dox}+I_{MB}$ values and photocurrents of the developed biosensing platform. $C_{miRNA-210} = 100$ pM.

13. Photocurrent stability of the biosensing platform

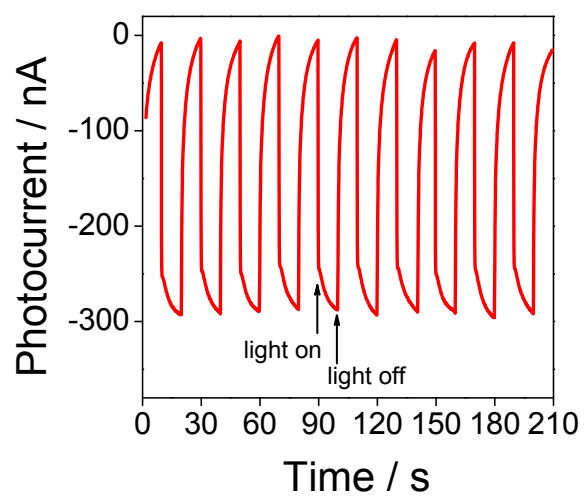


Figure S11. Photocurrent stability of the biosensing platform under 10 “on-off”

irradiation cycles. $C_{\text{miRNA-210}} = 100$ pM.

14. Comparison of different methods for miRNA-210 assay

Table S2 The comparison of the developed EC-PEC dual-mode biosensing platform with other methods for miRNA-210 assay.

Method	Detection limit	Linear range	Reference
EOF	10 fM	—	<i>Anal. Chem.</i> 2017 , <i>89</i> , 9201–9208
LBAS	1.39 pM	—	<i>J. Transl. Med.</i> 2020 , <i>18</i> , 108
Optics	0.78 nM	—	<i>J. Mater. Chem. B</i> 2020 , <i>8</i> , 4310–4317
Optics	9 fM	0–0.1 pM	<i>Analyst</i> 2015 , <i>140</i> , 1140–1148
LFNAB	85 pM	0.05–10 nM	<i>Sens. Actuators, B</i> 2018 , <i>264</i> , 320–326
FL	1.19 fM	1 fM–10 nM	<i>Analyst</i> 2019 , <i>144</i> , 4180–4187
EC	50 aM	0.5 fM–5 nM	<i>Biosens. Bioelectron.</i> 2021 , <i>178</i> , 113027
EC	0.28 fM	1 fM–1000 pM	<i>Analyst</i> 2021 , <i>146</i> , 4000–4009
EC	2.3 aM	0.01 fM–1 nM	Our work
PEC	18 aM	0.1 fM–1 nM	

EOF, Electroosmotic flow; LBAS, liquid bead array detection system; LFNAB, Lateral flow nucleic acid biosensor; FL, Fluorescence; EC, Electrochemistry; PEC, Photoelectrochemistry.

15. Recovery of miRNA-210 in the normal human serum samples

Table S3 Recovery of miRNA-210 in the normal human serum samples.

Sample	Added (pM)	Proposed EC method			Proposed PEC method		
		Found*	Recovery (%)	RSD (%)	Found*	Recovery (%)	RSD (%)
1	0.01	0.0101	101	2.9	0.00996	99.6	1.8
2	0.1	0.0975	97.5	3.6	0.104	104	4.7
3	1	0.982	98.2	1.5	1.03	103	2.1
4	10	10.2	102	1.7	9.76	97.6	1.6
5	100	103	103	2.2	102	102	4.3

*Each experiment was repeated three times.

16. Reference

- (1) Zeng, S.; Wang, S.; Xie, X.; Yang, S. H.; Fan, J. H.; Nie, Z.; Huang, Y.; Wang, H. H. Live-cell imaging of neurotransmitter release with a cell-surface-anchored DNA-nanoprism fluorescent sensor. *Anal. Chem.* **2020**, *92*, 15194–15201.
- (2) Xiao, K.; Meng, L. X.; Du, C. C.; Zhang, Q. Q.; Yu, Q.; Zhang, X. H.; Chen, J. H. A label-free photoelectrochemical biosensor with near-zero-background noise for protein kinase A activity assay based on porous ZrO₂/CdS octahedra. *Sens. Actuators, B* **2021**, *328*, 129096.
- (3) Mo, F.; Han, M.; Weng, X.; Zhang, Y. Y.; Li, J.; Li, H. B. Magnetic-assisted

- methylene blue-intercalated amplified dsDNA for polarity-switching-mode photoelectrochemical aptasensing. *Anal. Chem.* **2021**, *93*, 1764–1770.
- (4) Wang, Y. L.; Xia, L. Y.; Wei, C. Y.; Wang, H. H.; Wang, H. J.; Yuan, R.; Wei, S. P. Ultrasensitive photoelectrochemical microRNA biosensor based on doxorubicin sensitized graphitic carbon nitride assisted by a target-activated enzyme-free DNA walker. *Chem. Commun.* **2019**, *55*, 13082–13084.